Surface & Coatings Technology 438 (2022) 128419

Contents lists available at ScienceDirect

Surface & Coatings Technology

journal homepage: www.elsevier.com/locate/surfcoat

Designed Ti/TiN sub-layers suppressing the crack and erosion of TiAlN coatings

Haitao Ruan [b,c], Zhenyu Wang [a,c,*], Li Wang [a,c], Lili Sun [a,c], Hui Peng [d], Peiling Ke [a,c], Aiying Wang [a,b,c,*]

[a] Ningbo Institute of Industrial Technology, Ningbo 315201, China
[b] Center of Materials Science and Optoelectronics Engineering, University of Chinese Academy of Sciences, Beijing 100049, China
[c] Key Laboratory of Marine Materials and Related Technologies, Zhejiang Key Laboratory of Marine Materials and Protective Technologies, Ningbo Institute of Materials Technology and Engineering, Chinese Academy of Sciences, Ningbo 315201, China
[d] School of Materials Science and Engineering, Beihang University, Beijing 100191, China

ARTICLE INFO

Keywords:
Residual stress
Load-bearing capacity
Crack resistance
Erosion resistance

ABSTRACT

Solid particle erosion damage seriously affects the service life and operational safety of engine blades, while the erosion resistant coating is one of the effective measures to effectively improve the erosion resistance of the blade material and extend its service life. Here, we deposited the Ti/TiN/TiAlN multilayer coatings with different thickness ratio of the Ti to TiN layer on Ti-6Al-4V substrates by a home-made hybrid multisource cathodic arc system. The relationship between coating structure and coating properties including adhesion strength, residual stress, load-bearing capacity, crack resistance and erosion resistance was focused. Results showed that the Ti layer was beneficial in improving adhesion strength and reducing residual stress of the multilayer coatings, which was benefited from coordinating the deformation and absorbing strain energy induced by plastic deformation. The TiN layer was important in maintaining load-bearing capacity. Radial cracks initiation and propagation from the Ti/TiN interface occurred at most cases, while wide lateral cracks were formed only in the TiAlN layer for its high brittleness and internal stress during scratching. When the thickness ratio of the Ti to TiN layer was 1:2, the coating exhibited the best combination of hardness, adhesion strength, crack resistance, and load-bearing capacity. As a consequence, the coating behaved the lowest erosion rate of 0.060 ± 0.0002 mg/g and 0.024 ± 0.0068 mg/g at the erosion angle of 90° and 30°, respectively.

1. Introduction

During the operation of the aircraft, the compressed air carrying solid particles including sand, volcanic ashes, ice pallets, can be ingested into the engine and causes damage to the gas turbine compressor blades, called solid particles erosion (SPE) [1–3]. The maintenance cost, service life, and operational safety of the gas turbine were severely influenced by the SPE damage, and there was an urgent need for suitable methods to resist this damage [4,5]. Erosion resistant coatings, as a cost-effective and convenient protective strategy of the blades, were investigated and developed for several decades [6]. Up to now, metal/ceramic multilayer coating system was one of the most wildly studied coating system for its unique advantages, of which the combination of high toughness of metal and high hardness of ceramic contributed to better erosion resistance [7]. And thicker coatings could be easily manipulated benefiting from the lower and controllable internal stress, which was another advantage of the metal/ceramic multilayer coatings [8]. Thanks to the mature preparation process, various architecture designs were proposed, including Ti/TiN [9,10], Cr/CrN [11,12], TiAl/TiAlN [13], Cr/TiAlSiN [14], etc. The ductile metal layers of the multilayer coatings can absorb impacting energy and deflect the propagation of cracks by inducing plastic deformation, while the hard ceramic layers provide the resistance to erosion damage [12,15].

For the metal/ceramic multilayer coatings, the hardness [16] and adhesion strength [12,17] of the coating plays an important role in mechanical properties and erosion resistance. Shibe et al. [18] compared erosion resistance of the WC-12%Co and Cr_3C_2–25%NiCr cermet coatings and found the WC-12%Co coating, which owned higher hardness, exhibited better protection to the substrates. Naveed et al. [11] investigated the mechanical properties and erosion resistance of

* Corresponding authors at: Ningbo Institute of Industrial Technology, Ningbo 315201, China.
E-mail addresses: wangzy@nimte.ac.cn (Z. Wang), aywang@nimte.ac.cn (A. Wang).

https://doi.org/10.1016/j.surfcoat.2022.128419
Received 3 November 2021; Received in revised form 10 March 2022; Accepted 31 March 2022
Available online 4 April 2022

different structural coatings and concluded that the adhesion strength was one of the critical parameters and the higher adhesion strength was positive to improve the erosion resistance of the coating. While the high hardness was beneficial to the erosion resistance, residual stress would increase accompanying with the increasing of hardness, which promoted the formation of cracks under external force [19]. As a result, it was critical to reconcile the hardness and residual stress of the coatings. Besides, an appropriate architecture of the coatings can optimize the synergy of the ductile layer and the hard layer and reduced the residual stress [20]. Wieciński et al. [12] investigated the erosion properties of the Cr/CrN multilayer coatings, and the results showed that the presence of the Cr_2N transition layer provided a well-combined transition interface between the layers and avoided the appearance of lateral cracks and delamination. Whereas, in contrast to the most studies focused on multi-period multilayer coatings, Zhang et al. [21] surprisingly found that the TiN/Ti coating with one period exhibited better erosion resistance than that of the multilayer coatings with 2, 4, and 8 periods. High adhesion strength, fewer defects, and fewer hard layers were considered to be the key factors for better erosion resistance of the one period TiN/Ti coating, which indicated that there was no direct relationship between the periods and erosion resistance of the coatings. Our previous work also found that the improvement of the erosion resistance was not proportional to the cycles of the Ti/TiAlN layer [22], which was closely related to the hardness and thickness of the TiAlN layer. What's more, the interface of the multilayer coating played an important role in suppression the propagation of the cracks [15]. Owing to the hardness gap of the Ti and TiAlN layer, delamination was detected near the interface of the coating and the substrate after erosion and lateral cracks were observed in the coatings, which limited the improvement of the erosion resistance. And the sharp interface between the ductile layer and the hard layer affected the erosion resistance of the multilayer coating to a great extent [23], which was also proved in Ref. [24,25]. In this study, the material selection and architecture design were aimed at better cohesion strength in the coatings and reducing residual stress of the coatings, while maximizing the hardness, adhesion strength and load-bearing capacity.

The TiAlN coating, which was widely applied as erosion resistance coatings for its high hardness, superior erosion resistance and high thermal stability [26–28], was chosen as the hard layer in our previous work [22]. But one of its major defects is poor resistance to brittle fracture. Yang et al. [29] deposited the TiAlN coatings by reactive magnetron sputtering and demonstrated that the TiAlN coatings exhibited the best erosion resistance, which were several times higher than that of TiN coatings. Deng et al. [30] fabricated four nitride coatings (CrN, TiN, CrAlN, and TiAlN) and examined corresponding comprehensive properties, the results showed that the TiAlN coating owned the best erosion resistance. For the metallic layer materials, Ti layer can improve interfacial transition between the coating and the Ti-6Al-4 V substrate and decrease the internal stress of the coating [31]. Besides, the hardness of the TiN layer is between the Ti layer and the TiAlN layer, which is an ideal transition material between Ti and TiAlN.

In this study, Ti/TiN/TiAlN multilayer coatings with different thickness ratios of the Ti to TiN layer were deposited on Ti-6Al-4V substrates by a home-made hybrid multisource cathodic arc ion deposition system. The Ti layer as joint layer provides strong adhesion to the substrates and reduces the residual stress of the coating, while the TiN layer with moderate hardness plays a role as transition layer of the Ti layer and TiAlN layer to ensure the gradient of hardness and the TiAlN layer assumes the main role of erosion resistance by the virtue of its excellent mechanical properties. The results here can provide a fundamental understanding of enhanced erosion resistance by multilayer architecture.

2. Experimental details

2.1. Coating deposition

Titanium alloys of Ti-6Al-4V (TC4) with a dimension of 30 mm × 10 mm × 3 mm were employed as substrates for this study. All substrates were mechanically polished to 3000 grit by SiC abrasive papers and ultrasonically cleaned in acetone and ethanol for 5 min and 15 min before deposition, respectively. The Ti/TiN/TiAlN multilayer coatings were deposited by a home-made multisource cathodic arc evaporation system, as illustrated in Fig. 1. Ti targets (for the Ti joint layers and TiN transition layers; purity: 99.9 wt%) and TiAl targets (for the TiAlN layers, purity: 99.9 wt%) with an atomic ratio of 33:67 were applied as cathodes. During the deposition process, the chamber was kept a base pressure lower than 3.0×10^{-5} Torr and the temperature was kept at 300 ± 10 °C. Before the deposition, the substrates were etched by Ar ions for 30 min with a negative bias of 200 V to remove impurities attached to the surface and the targets were pre-sputtered for 3 min for self-cleaning. At the beginning of the deposition, high negative bias was applied on substrates for high-energy Ti ions bombardment to enhance the adhesion strength between the coating and the substrate for 3 min. Subsequently, Ti layer, TiN layer and TiAlN layer was successively deposited in front of the respective target in Ar atmosphere, N_2 atmosphere, and N_2 atmosphere with a negative bias of 70 V, 70 V, and 80 V, respectively. During all above cleaning and deposition processes, the sample holder kept rotating clockwise. Detailed process parameters are shown in Table 1 and the total thickness of the Ti/TiN/TiAlN multilayer coatings in this study were kept around 10.0 μm. A set of samples without Ti joint layer was marked as G1, the samples with different thickness ratio of the Ti to TiN layer were marked as G2 to G5 and the G6 samples were without TiN transition layer. The detailed information is shown in Table 2. The deposition time of the Ti layers was set as 14 min, 24 min, 36 min, 54 min, and 72 min corresponding to the G2-G6 samples, respectively. And the deposition time of the TiN layers was 100 min, 80 min, 66 min, 50 min, and 25 min corresponding to the G1-G5 samples, respectively. Besides, the deposition time of the TiAlN layers of all samples was kept as 122 min.

2.2. Scratch tests

The adhesion strength of the coating to the substrate was determined by scratch tests using CSM Revetest (Switzerland) equipped with a diamond Rockwell conical indenter (apex angle of 120° and curvature radius of 200 μm). During the progressive scratch test, the indenter was loaded continuously from 1 N to 100 N and the scratch length, scratch speed was 3.00 mm, 1.00 mm/min, respectively. The load was kept as 10 N, 30 N, and 50 N in the constant load scratch test, respectively, while the other parameters were kept the same as the progressive scratch test. Each sample was employed at least 3 tests to require accurate results.

2.3. Nanoindentation tests

The hardness and elastic modulus of the as-deposited coatings were determined using nanoindentation (Nano Indentation G200, MTS, USA) with a Berkovich-diamond tip in continuous stiffness measurement (CSM). In order to avoid the influence of the metallic macro-particles on the test results, all samples applied to the tests were polished by ball-cratering apparatus. Six random indents were performed on each sample. The model of Oliver and Pharr [32] was used to calculate the values of hardness and elastic modulus.

2.4. Erosion tests

The erosion tests were performed at room temperature by a home-made test rig following the ASTM G76-13 standard with angular silica (SiO_2, ~61 μm) sand as erosion particles, the schematic diagram of the

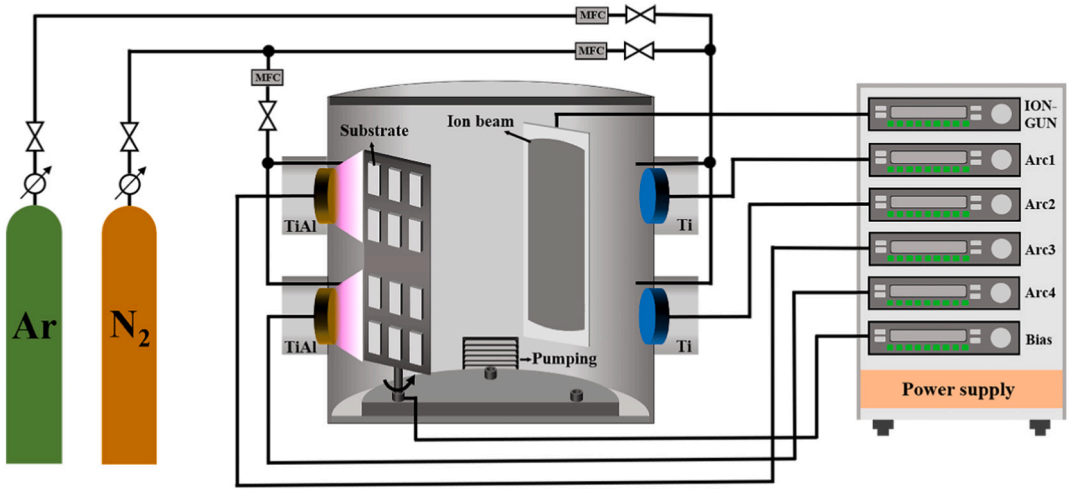

Fig. 1. Schematic diagram of the coating deposition system.

Table 1
Process parameters of cleaning and deposition.

Procedure	Current (A)			Ar flow (mL/min)	N_2 flow (mL/min)	Chamber pressure (mTorr)	Negative bias (V)
	Ion beam	Ti cathodes	TiAl cathodes				
Ion etching	0.2	–	–	35.0	–	1.5	200
Ti ion bombardment	–	70	–	200.0	–	45.0	400
Ti layer	–	70	–	200.0	–	45.0	70
TiN layer	–	70	–	–	500.0	45.0	70
TiAlN layer	–	–	70	–	550.0	54.5	80

Table 2
Structure design of Ti/TiN/TiAlN multilayer coatings.

Group	Ti layer (μm)	TiN layer (μm)	TiAlN layer (μm)	Thickness ratio of Ti to TiN layer (T_{Ti}:T_{TiN})
G1	/	6.0	4.0	/
G2	1.2	4.8	4.0	1:4
G3	2.0	4.0	4.0	1:2
G4	3.0	3.0	4.0	1:1
G5	4.5	1.5	4.0	3:1
G6	6.0	/	4.0	/

test rig was shown in Ref. [22]. A tungsten carbide nozzle with an inner diameter of 1.5 mm and a length of 20 mm was applied in the tests. During the erosion tests, the distance between sample surface to the nozzle, erosion angle, compressed air pressure, the feed rate and total mass of erosion particles were kept at 20 mm, 90° and 30°, 0.2 MPa, 2.0 ± 0.1 g/min and 10.0 ± 0.5 g, respectively. Before and after the erosion test, samples used in erosion tests were ultrasonically cleaned with ethanol for 15 min to remove impurities and residual erodent and then dried by high-pressure nitrogen. An analytical balance with a resolution of 0.01 mg (Mettler Toledo, XS205 DU) was used to determine the mass change of the samples before and after the erosion test. The erosion rate was determined according to the Eq. (1). At least three tests for each sample were conducted to enhance the quality of statistics.

$$\text{Erosion rate (ER)} = \frac{\text{Mass loss of the specimen (mg)}}{\text{total mass of particles (g)}} \quad (1)$$

2.5. Characterization of the coatings

A field-emission scanning electron microscopy (SEM, FEI Quanta FEG 250) was applied to observe the surface and cross-section morphology of the as-deposited and the scratch tracks, and the chemical composition of the coatings was determined with the energy-dispersive X-ray spectroscopy (EDS) at an accelerating voltage of 20 kV, which is attached on the SEM.

The preparation of the cross-sectional of the samples were cut by a low-speed saw (IsoMetTM, Buehler, USA), then ultrasonically cleaned with ethanol for 10 min and polished by a broad ion beam system (BIB), using Leica EM TIX 3X at the milling voltage of 7 kV.

The crystal structure of the as-deposited Ti/TiN/TiAlN multilayer coatings was analyzed by X-ray diffraction (XRD, Bruker D8 DISCOVER, Germany) with a diffractometer using Cu K_α radiation (wavelength 1.5406 Å) operating at 42 kV and 100 mA. The Grazing Incidence XRD was analyzed using Bruker D8 ADVANCE DAVINCI (Germany), where the incident angle used for GIXRD measurements was set 0.5°.

The residual stress of the as-deposited Ti/TiN/TiAlN multilayer coatings was measured using a Bruker D8 Discover X-ray diffractometer equipped with a Vantec-500 2D detector, which operated with a characteristic Cu Kα radiation source with a wavelength (λ) of 1.541 Å. An accelerating X-ray voltage of 40 kV and beam current of 40 mA were used. The stress measurement is based on the relationship between the stress tensor and the diffraction cone distortion. When the deposited coating exists the tensile or compressive residual stress, the crystal planes of the grains with different orientations are stretched or compressed, resulting in the change of interplanar spacing. In this case, the diffraction peaks generated under Bragg diffraction will shift upwards or downwards accompanied with the changes in interplanar spacing. According to the changes of diffraction peaks, the residual stress can be estimated for the sample. More detailed description was illustrated in Ref. [33].

3. Results and discussion

3.1. Morphology and chemical composition

The cross-section morphologies of the as-deposited coatings with

different Ti/TiN thickness ratios were observed using SEM, as shown in Fig. 2. For all coatings, interfaces between the single layers were clear and the coatings bonded well with the substrates. In addition, the layers within the coatings showed a good adhesion, without any cracks, gaps, or other defects. The total thicknesses of the as-deposited coatings for G1-G6 samples were measured to be 8.5 μm, 10.1 μm, 9.1 μm, 8.4 μm, 10.0 μm and 9.6 μm, respectively. For the Ti joint layers of G2-G6 samples (Fig. 2(b)-(f)), the thickness was measured to be 1.2 μm, 1.6 μm, 2.3 μm, 4.4 μm and 5.3 μm, respectively; while the thickness of the corresponding TiN transition layers of G1-G5 samples was measured to be 4.6 μm, 4.3 μm, 3.2 μm, 2.3 μm, and 1.2 μm, respectively. It needed to note that the thickness variety of the TiAlN layers from 3.9 μm to 4.8 μm was caused by the fluctuation of the deposition rate under the same deposition conditions. The EDS line scanning also shown obvious differences in distribution of elements in each layer of the coatings. Atomic percent of the chemical coating composition was also quantitatively given in Table 3 and the EDS measurements confirmed the compositional features of the coating. It needed to noted that the EDS technology was weak sensitivity in detecting light elements [34], such as nitrogen. In addition, the concentration of carbon and oxygen was neglected owing to its low content and irrelevance for this study, although it was detectable. However, the results here could help discern the coating structure.

3.2. Crystal structure

X-ray diffraction was employed to investigate the phase structure of the as-deposited Ti/TiN/TiAlN multilayer coatings. As shown in Fig. 3 (a), the visible peaks were proved to be (100), (002), (101), (102), (110), (103), (200), (112), (201) planes of pure Ti phase. Meanwhile, the intensity of all Ti diffraction peaks became higher and sharper as the thickness of the Ti layer increasing. Besides, Ti (101) plane became dominant comparing to the other Ti peaks with the increased thickness of the Ti layer, indicating that the coatings with thicker Ti layer exhibited the preferred orientation of (101) plane. For the Ti/TiN/TiAlN multilayer coatings, the peak of the TiN (111) became weaker with the decrease in the thickness of TiN layer, while the peak intensity of TiN (200) exhibited a relatively small change. Moreover, noted that the peak of TiN (111) and (200) plane shifted towards lower 2θ angle and higher 2θ angle for the G1 to G5 samples, while the TiN (111) and (200) plane of the G6 sample both shifted towards higher 2θ angle. The coatings deposited by physical vapor deposition were usually accompanied with compressive stress, which was caused by the atomic peening effect [25]. This compressive stress would lead the diffraction peaks of TiN phase to shift to lower 2θ angle [35]. The TiAlN phase was formed by substituting Ti atoms in the TiN lattice with Al atoms which has smaller atomic radius compared to Ti atoms [13,36,37], and thereby led to shrinkage in the lattice parameter and accompanied by a shift of the diffraction peaks towards to higher 2θ angle. Besides, the TiN and TiAlN phases corresponded to the same specification of the XRD maps (PDF#38-1420). As a result, the peak of TiN (111) plane was dominated by TiN phase and the peak of TiN (200) plane was dominated by TiAlN phase for the G1 to G5 samples. The peaks of TiN (220), (311) and (222) plane were assigned to the combination of TiN phase and TiAlN phase for the G1 to G5 samples. Fig. 3(b) showed the GIXRD patterns of as-deposited, the diffraction peaks of TiN (111), (200) and (220) exhibited obvious shift to higher 2θ angle, which proved the existence of TiAlN phase. Different from G1 to G5 samples, the diffraction peaks of TiN (111) and (200) for the G6 sample were weak and smooth, which may be caused by the absence of the TiN layer. Combined with the cross-sectional morphologies and EDS measurement, it was further confirmed the structure of the as-deposited coatings.

Table 3
Atomic percent of the chemical composition of Ti/TiN/TiAlN multilayer coatings.

	TiAlN layer			TiN layer		Ti layer
	Ti/at.%	Al/at.%	N/at.%	Ti/at.%	N/at.%	Ti/at.%
G1	21.06	34.61	42.76	58.70	35.48	/
G2	22.01	35.57	41.21	57.24	39.10	94.83
G3	22.43	34.09	40.78	59.43	39.79	95.33
G4	21.89	34.20	41.71	57.16	38.31	95.15
G5	22.01	35.25	41.51	57.94	37.72	95.81
G6	21.33	35.36	41.99	/	/	94.79

3.3. Mechanical property

3.3.1. Residual stress

Residual stress was detected and shown in Fig. 4. All samples exhibited the state of compressive stress and the value decreased from

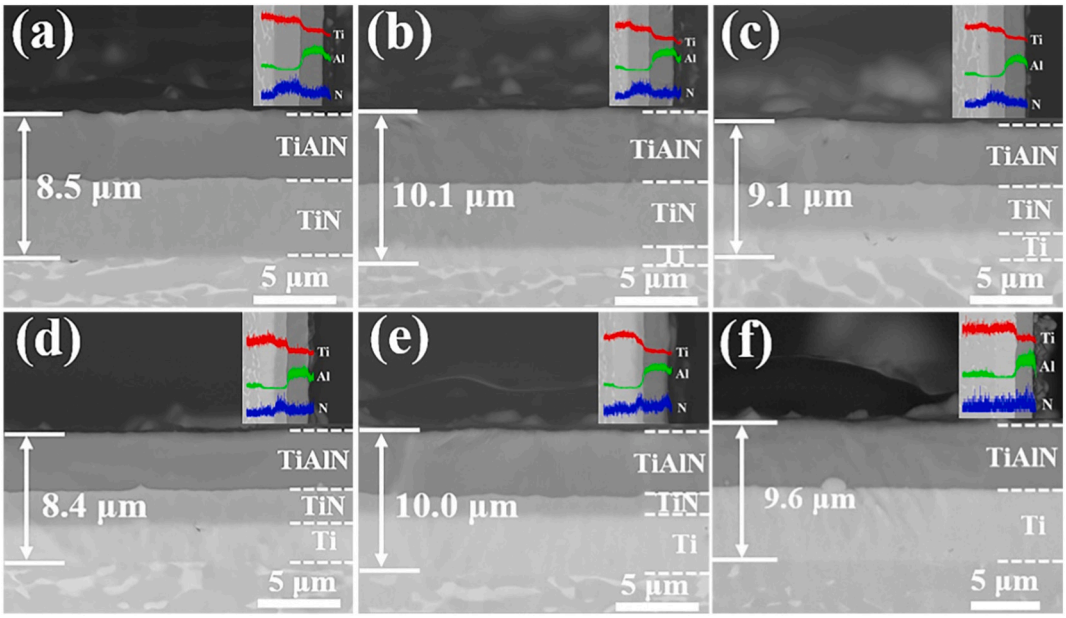

Fig. 2. (a)-(f) SEM images and EDS line scanning of cross-sections of the as-deposited coatings, corresponding to the G1-G6 samples, respectively.

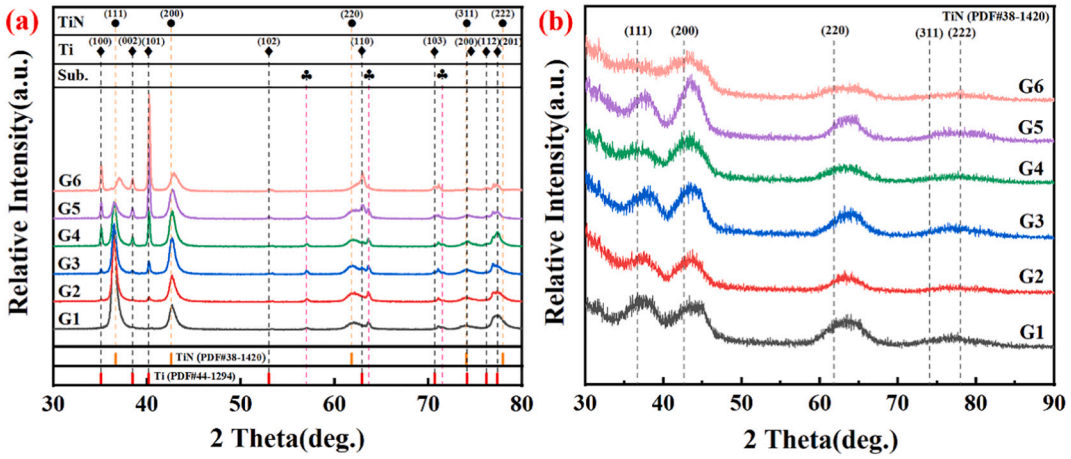

Fig. 3. (a) The XRD patterns of as-deposited coatings, (b) The GIXRD patterns of as-deposited coatings.

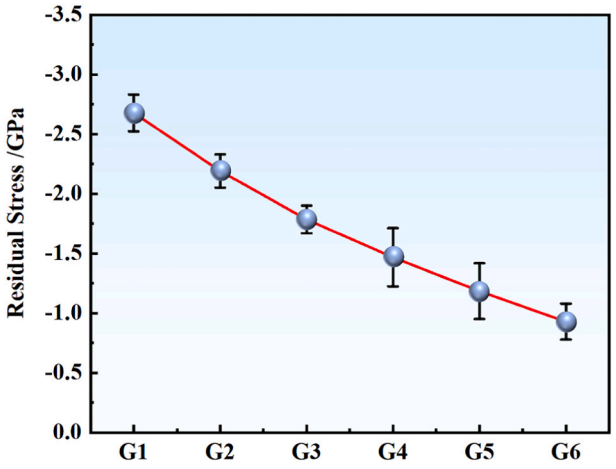

Fig. 4. Residual stress of the as-deposited various Ti/TiN/TiAlN multilayer coatings.

-2.68 ± 0.15 GPa (the G1 sample) to -0.93 ± 0.15 GPa (the G6 sample) with the thickness of Ti layer increased, indicating that the Ti layer was beneficial in reducing the residual stress of the coatings.

3.3.2. Hardness and elastic modulus

Mechanical properties including hardness and elastic modulus of the as-deposited Ti/TiN/TiAlN multilayer coatings were determined by nanoindentation. To avoid the influence of the substrates on the hardness of the coatings, the indentation depth was controlled within one tenth of the total thickness of the coatings [38]. As a result, the indentation depth was controlled at 1000 nm for all samples and the forces used for each sample were varied from approximately 190 N to 400 mN for the G6 to G1 samples, respectively. To clarify the effect of Ti and TiN layer on the multilayered coatings, the nanoindentation test was performed further for each individual layers including Ti, TiN and TiAlN. Fig. 5(a) shows the hardness and elastic modulus of each layer. The hardness of Ti, TiN and TiAlN layers embedded in the multilayered coatings were 3.7 ± 0.6 GPa, 27.2 ± 0.4 GPa and 38.8 ± 1.7 GPa, respectively. In addition, different with the lower elastic modulus of Ti at 137.7 ± 12.5 GPa, both the individual TiN and TiAlN layers displayed the higher elastic modulus at 375.8 ± 27.2 GPa and 627.9 ± 19.3 GPa. Therefore, it could be said that inserting the softer sub-layers both of Ti and TiN with the same TiAlN top layer decreased the average hardness and elastic modulus of multilayered coatings in terms of the evolution of residual stress. As shown in Fig. 5(b), the hardness and elastic modulus of all coated samples ranging from 38.7 ± 0.5 GPa to 25.7 ± 0.9 GPa and 508.9 ± 17.6 GPa to 267.8 ± 16.6 GPa, respectively, which were at least 3–6 times larger than that of the pristine substrate (6.5 ± 0.8 GPa and 164.3 ± 26.9 GPa). As the thickness of Ti layer increasing, the hardness of the coatings gradually decreased from 38.7 ± 0.5 GPa (the G1 sample) to 25.7 ± 0.9 GPa (the G6 sample) and the elastic modulus gradually decreased from 508.9 ± 17.6 GPa (the G1 sample) to 267.8 ± 16.6 GPa (the G6 sample). It was because the increasing the thickness of Ti layer led to the decrease of the residual stress of multilayer coatings, which thereafter lowered the test hardness. Most importantly, noted that the absence of TiN sub-layer in G6 sample caused the significant decrease of hardness to 25.7 ± 0.5 GPa together with the lowest residual

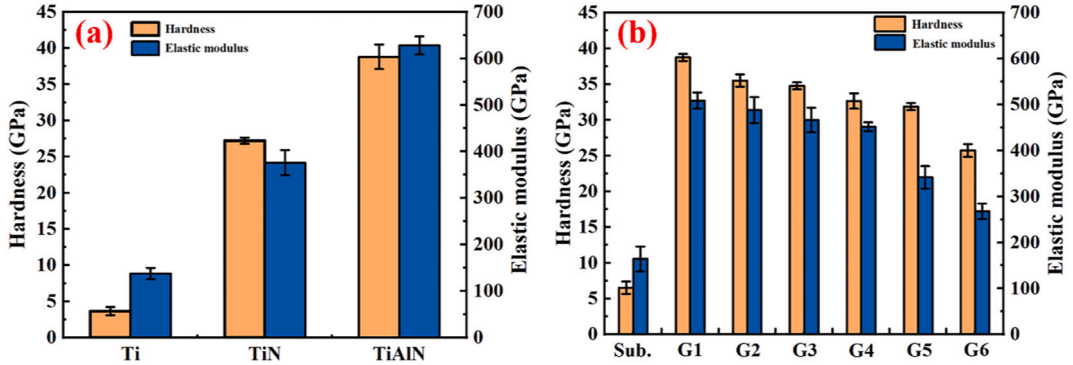

Fig. 5. Hardness and elastic modulus of (a) Ti, TiN, TiAlN individual layer embedded in multilayered coatings, (b) the substrate and the Ti/TiN/TiAlN multilayer coatings.

stress.

3.3.3. Adhesion strength

Fig. 6 shows morphologies of the scratch tracks of the as-deposited coatings and the adhesion strength is given in the figures. The adhesion strength (i.e. critical load) was defined as the load which was corresponded to the complete and continuous delamination events with large area exposure of the substrate [22]. As shown in Fig. 6(a), the G4 sample exhibited the highest adhesion strength (70.1 ± 1.3 N). Compared to the G1 sample (without Ti layer), the presence of the Ti layer could absorb strain energy during the deformation process and provide better adhesion between the substrates and the coatings, and thereby significantly improved the adhesion strength of the as-deposited coatings. The degradation of the adhesion strength of the G5 and G6 samples were presumed to be the reduced load-bearing capacity of the coatings with thinner TiN layer.

Apart from adhesion strength, morphologies of the scratch tracks also exhibited obvious distinction, as shown in Fig. 6(b)–(g) and Fig. 6 (h)-(m), which were the corresponding enlarged images of the framed area in Fig. 6(b)-(g), respectively. In the initial stage of the scratch process of the G1 sample, chipping events could be detected at the edge of the scratch track as a consequence of its poor crack resistance, indicating that the coatings were possessed of high internal stress, as shown in Fig. 6(b). When the load was approximately 50 N, the substrates of the G1 sample were completely exposed and large area peel-off events occurred at the edge of the scratch track. According to the corresponding enlarged image shown in Fig. 6(h), the peel-off area showed the brittle nature with river-like-pattern appearance, suggesting that the cracks initiated at the edge of the scratch edge [15]. The coating of the G1 sample exhibited typical adhesive failure feature, accompanied with cohesive failure at the edge of peeling area. As a comparison, cracks at the edge of scratch track appeared at higher load in the G2 sample (Fig. 6 (c)). Few adhesive failure and cohesive failure could be detected along the edge of the scratch track of the G2 sample, indicating the better coating-substrate adhesion. Besides, obvious delamination occurred in the middle of the scratch track while the load was approximately 45 N (Fig. 6(i)), which proved that higher inter-layer adhesion strength could be pursued. As the thickness of the Ti layer increased, the G3 and G4 samples both behaved well adhesion to the substrate with few cohesive failure occurred, and no adhesive failure was detected, as shown in Fig. 6(d)-(e) and Fig. 6(j)-(k), respectively. However, when the thickness of the Ti layer further increased, the contribution of the TiN layer to the load-bearing capacity of the coating became diminishable. For this reason, the exposion of the substrates for the G5 and G6 samples were found at lower load than that of the G4 sample (Fig. 5(f)-(g)). Besides, few cohesive failure events could be observed and more debris appeared at the edge of the scratch track (Fig. 6(l)), and only small area of spalling was detected in the scratch track of the G6 sample (Fig. 6(m)). As a consequence, the Ti layer played a key role in improving the adhesion strength, reducing internal stress, and absorbing strain energy by inducing plastic deformation. The TiN layer was essential to maintain the load-bearing capacity of the coating, which was the premise and

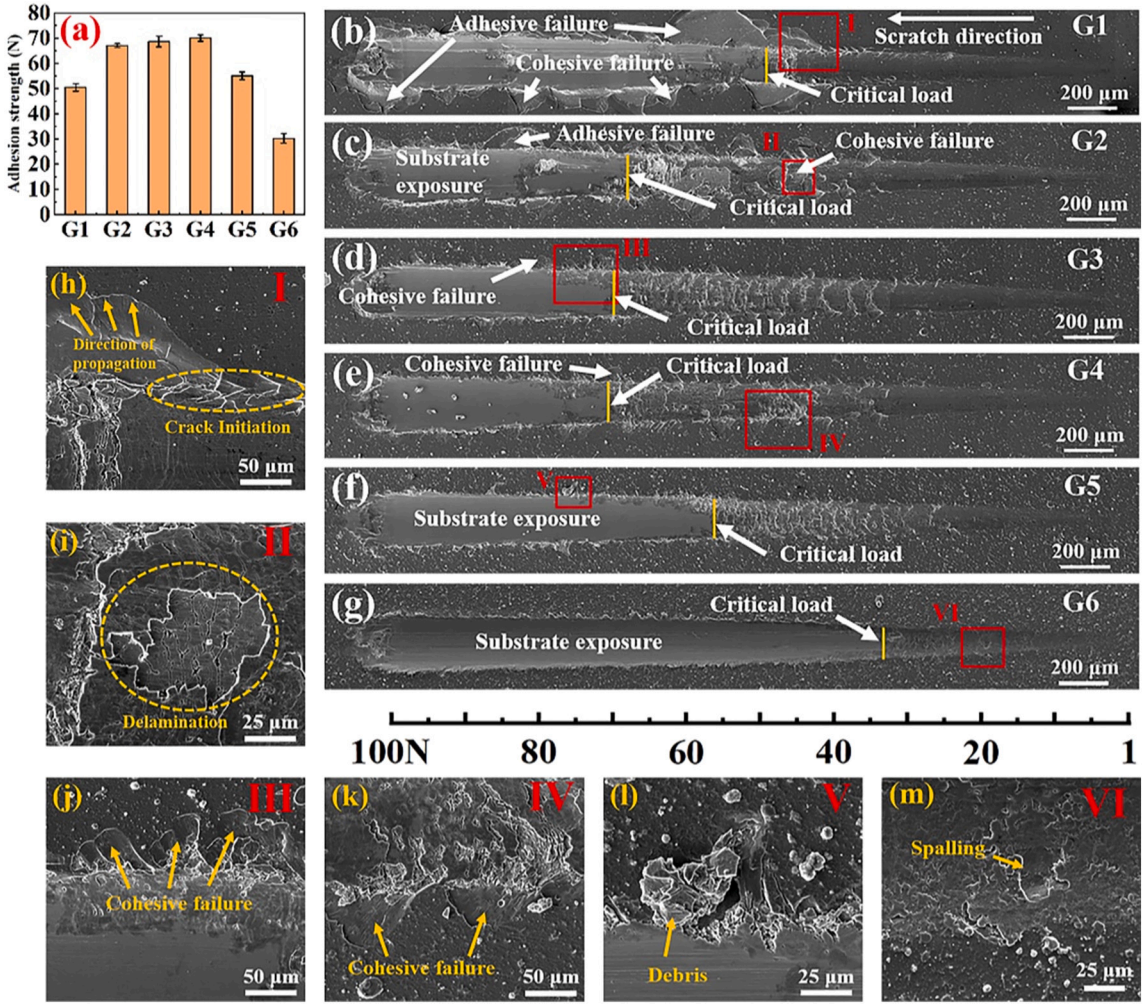

Fig. 6. (a) The adhesion strength of the as-deposited coatings, (b)– (g) scratch morphologies of the Ti/TiN/TiAlN multilayer coatings, (h) – (m) enlarged images of the framed area in Fig. 6(b) - (g), respectively.

basis to the improvement of adhesion strength.

3.3.4. Crack resistance

The generation and propagation of cracks were empirically considered as one of the key factors for the erosion failure in hard brittle coating. Therefore, the crack resistance of multilayer coatings was particularly focused to elucidate the crack generation and the caused coating failure. Fig. 7 shows the cross-sectional morphologies of the middle scratch track during test at constant load of 10 N, 30 N, and 50 N, respectively.

The cross-sectional micrographs of the scratch tracks of the Ti/TiN/TiAlN multilayer coatings beneath the tip of the indenter under the load of 10 N are illustrated in Fig. 8. As the result of large difference of deformation between the soft substrate and hard coating, the evidence of delamination was observed at the substrate/coating interface for the G1 sample after the scratch test, indicating the poor adhesion of the coating/substrate interface (Fig. 8(a)). Thanks to the existence of the Ti layer, which had similar mechanical properties to the substrate, all other coatings (Fig. 8(b)-(f)) exhibited well transition of coating/substrate interface and strong adhesion to the substrates. Besides, all radial cracks initially generated at the Ti/TiN interface and propagated towards the surface of the G1 to G5 samples (Fig. 8(b)-(e)), indicating that the stress induced by the plastic deformation exceeded the fracture toughness of the coating. With the thickness of the Ti layer increasing, the number and length of radial cracks increased. The G4 and G5 samples had similar crack number and size (Fig. 8(d)-(e)), which indicated that the plastic deformation of the coatings reached the maximum degree under the load of 10 N. The G6 sample emerged radial cracks with larger size, which penetrated the TiAlN layer, indicating the poor load-bearing capacity of the coating and sharp interface of the Ti to TiAlN layer. Besides, the energy induced by plastic deformation exceeded the tolerance under that the thin Ti layer can withstand for the G2 sample, and fine lateral crack, which caused by shear stress and high residual stress, was formed within the TiAlN layer (Fig. 8(b)). The existence of the thick Ti layer averted the formation of fine lateral cracks by absorbing energy during the scratch test and reducing the residual stress of the coatings.

As the load of scratch tests increasing to 30 N, the discrimination of the crack resistance of the coatings became obvious, as shown in Fig. 9. Plastic deformation of the substrate induced by the normal compressive stress under applied normal load during the scratch test would cause bending stress in the coating, which was responsible for initiation and propagation of the radical cracks [15,39,40]. In this case, stress states of the coating were different at the upper and lower layers, which corresponded to the compressive stress and tensile stress, respectively [41,42]. Compared to the case of 10 N, obvious lateral cracks were detected within the TiAlN layer of the G1 sample and radial cracks formed at the TiN/substrate interface. While some cracks were suppressed in the TiN layer or blocked by lateral cracks in the TiAlN layer, and the others penetrated though the coating (Fig. 9(a)). As for the G2 sample (Fig. 9(b)), the Ti layer enhanced the fracture toughness of the coating and reduced the number of radial cracks by harmonizing the deformation between the substrates and the coatings. However, lateral cracks were detected in both TiN layer and TiAlN layer, which can be explained by the fact that the Ti layer was too thin to fully perform its function. As the thickness of the Ti layers increase, radial cracks initiated at the Ti/TiN interface or formed from the metallic macroparticle, without any lateral cracks or delamination (Fig. 9(c)). Besides, the size (length and width) of radial cracks in the G3 sample were smaller than that of the G2 sample, indicating that the G3 sample had better crack resistance by better coordinating deformation and absorbing stress. The G4 sample had the same number of radial cracks as the G3 sample, but their size was larger than that of the G3 sample (Fig. 9(d)). Noted that one of the cracks was initiated at the TiN/TiAlN interface, which was presumably due to the decrease of the thickness of TiN layer that caused the deterioration of the load-bearing capacity, resulting in greater deformation and the change of initial position of the crack. For the G5 sample, the load-bearing capacity of the coating was further degraded, fine lateral cracks and radial cracks were observed in both TiN and TiAlN layers, as shown in Fig. 9(e). Apart from that, large penetrative radial cracks could also be observed in the G5 sample. When the thickness of the Ti layer reached maximum value for the G6 sample, obvious plastic deformation was occurred and the coating peeled off Fig. 9(f), which was consistent with its low adhesion strength. In summary, it was found that all Ti layers under the load of 30 N remained intact without any cracks and provided a strong coating-substrate adhesion, except for the G1 and G6 sample. The transition of the TiN/TiAlN interface was better than that of the Ti/TiN interface, and the presence of the Ti layer was beneficial in reducing the internal stress of the coatings. Besides, the load-bearing capacity of the coatings had a great influence in initiation and propagation of cracks.

At the last step, the crack evolution of the coatings under the load of 50 N can be obtained from Fig. 10. For the G1 sample (Fig. 10(a)), chipping events occurred in the TiAlN layer, and shear behavior penetrated through the coatings was observed, indicating that the induced shear and bending stress exceeded the fracture toughness of the coating [15]. Lateral cracks, radial cracks, and fragmentation were also detected in the coating, accounting for the poor crack resistance of the coating. With the emergence of the Ti layer, shear and fragmentation phenomenon disappeared (Fig. 10(b)), which was profit from the deformation coordination and energy absorption of the Ti layer. Because of the relatively high brittleness of the TiN and TiAlN layers and the thin thickness of the Ti layer, chipping events were detected along with lateral and radial cracks. When the thickness of the Ti layer increases, only wide lateral cracks and radical cracks could be observed in the coating (Fig. 10(c)). A thick Ti layer could afford better fracture toughness to resist deformation and the ability of energy absorption. As for the G4 sample, the behavior of lateral and radial cracks was similar to that of the G3 sample. Due to the presence of a thicker Ti layer, the coating exhibited more obvious plastic deformation (Fig. 10(d)), indicating its worse load-bearing capacity than that of the G3 sample. The coatings of the G5 and G6 sample were totally peel off under the load of 50 N and only part of the Ti layer adhered to the substrate (Fig. 10(e)-(f)). And obvious plastic deformation taken place, showing the worst load-bearing capacity of the coating. Expect for the G1, G5 and G6 sample, the Ti layer in the coatings remained intact and only the plastic deformation occurred. Based on the scratch test under the load of 10 N, 30 N, and 50 N, it was reasonable to conclude that the G3 sample had the best combination of crack resistance performance and load-bearing capacity. Combined with the previous results, the Ti/substrate interface remained good and radical cracks were generated at the Ti/TiN interface in the vast majority of cases. This indicated that the transition of the Ti/substrate and TiN/TiAlN interfaces were satisfactory, while the transition of Ti/TiN interface remained to be further optimization.

According to the above results and discussion, it could be concluded the Ti and TiN layer played an important role in enhancement of the crack resistance. In the Ti/TiN/TiAlN multilayer coatings, the Ti layer

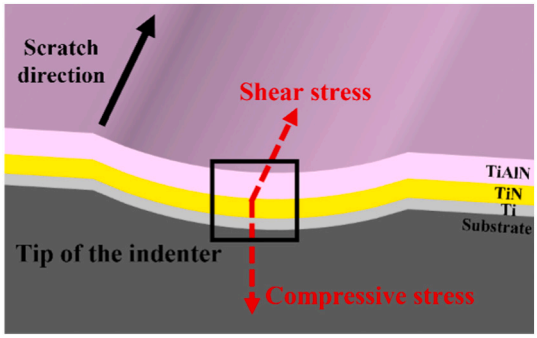

Fig. 7. Schematic of the scratch track.

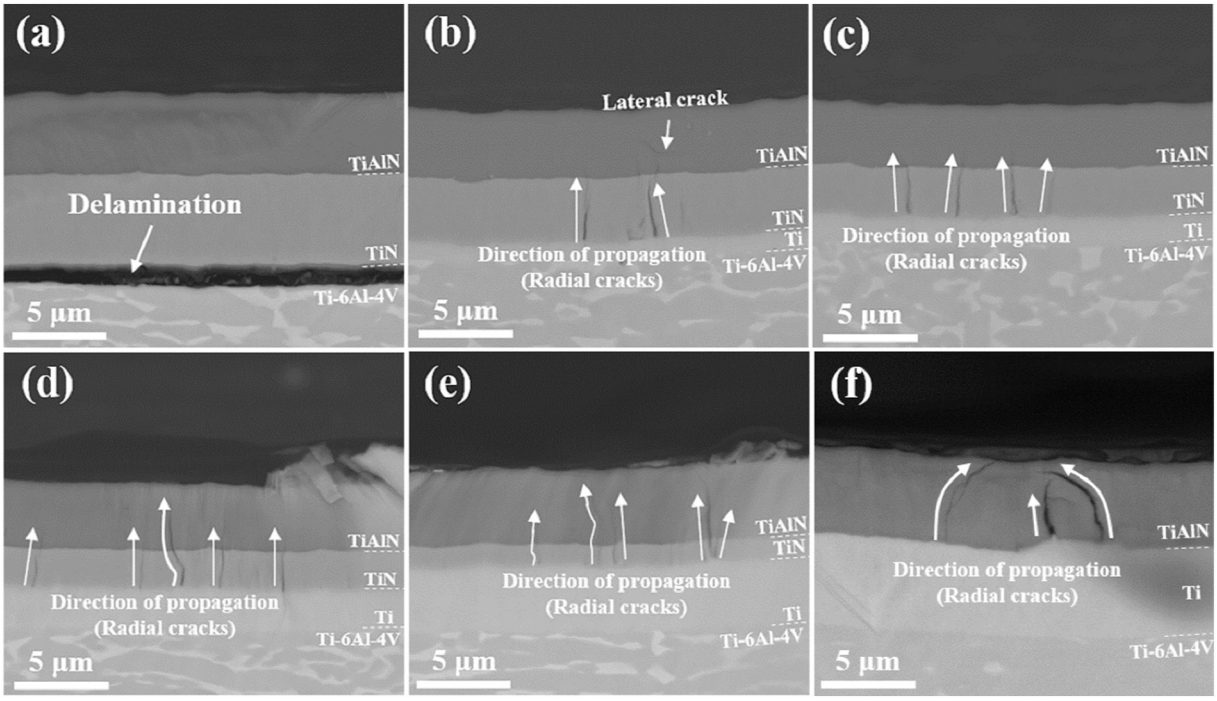

Fig. 8. Cross-sectional SEM images of the Ti/TiN/TiAlN multilayer coatings after scratch tests at the area beneath the tip of indenter at 10 N. (a) – (f): G1-G6 sample, respectively.

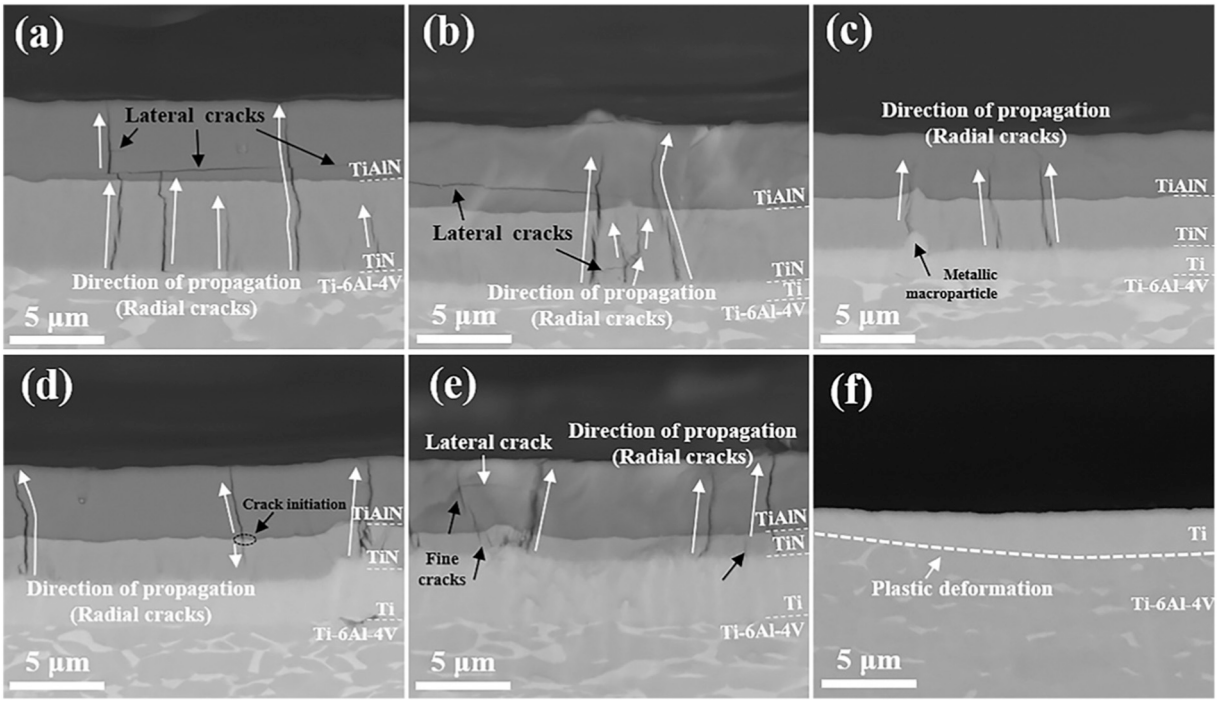

Fig. 9. Cross-sectional SEM images of the Ti/TiN/TiAlN multilayer coatings after scratch tests at the area beneath the tip of indenter at 30 N. (a) – (f): G1-G6 sample, respectively.

works as a buffer, reducing the residual stress, coordinating the deformation between the soft substrate and the hard TiN/TiAlN layer and absorbing energy caused by deformation. What's more, proper Ti layer could improve the adhesion strength between the coating and the substrate. The TiN layer was pivotal to the load-bearing capacity of the coatings, which influenced the crack resistance to a great extent. Failure mechanism of the Ti/TiN/TiAlN multilayer coating is proposed, as presented in Fig. 11.

3.4. Erosion resistance

Fig. 12 illustrates the erosion rates of the pristine Ti-6Al-4V substrates and the Ti/TiN/TiAlN multilayer coatings eroded by silica sand under the erosion angle of 90° and 30°. Owing to the improvement of the

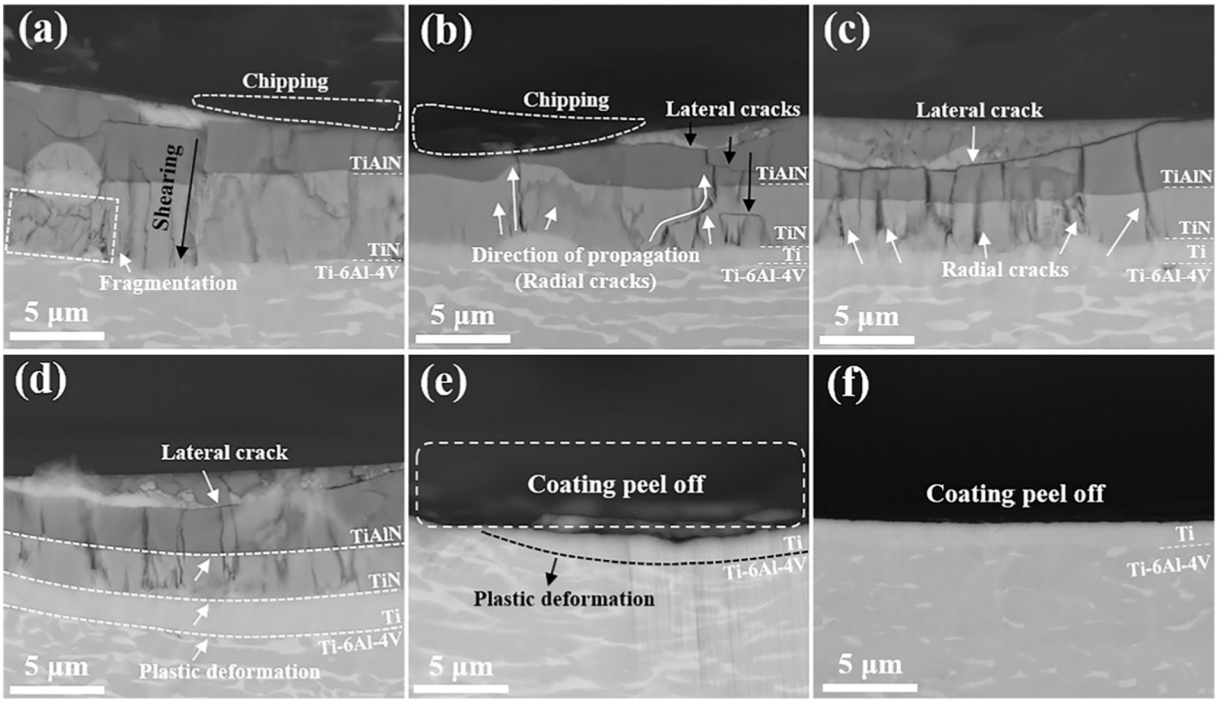

Fig. 10. Cross-sectional SEM images of the Ti/TiN/TiAlN multilayer coatings after scratch tests at the area beneath the tip of indenter at 50 N. (a) – (f): G1-G6 sample, respectively.

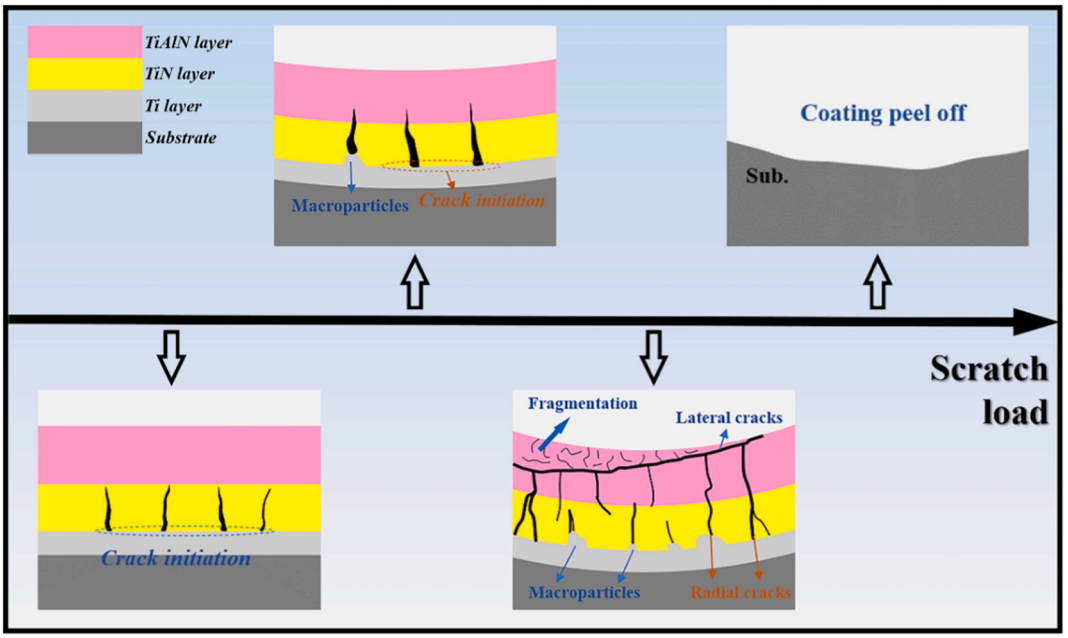

Fig. 11. Schematic illustrations of crack evolution and failure mechanism of the Ti/TiN/TiAlN multilayer coating.

mechanical properties of the samples' surface, all coated samples exhibited much lower erosion rates compared to the pristine substrate. The erosion rates of the substrates were 0.446 ± 0.0243 mg/g and 0.496 ± 0.0508 mg/g, under 90° and 30°, respectively. For the erosion failure of G1 sample, one reason was that the poor adhesion strength stimulated the interface delamination under erosion test, which thereafter deteriorated the erosion resistance significantly. Another key factor was due to the observed higher residual stress without Ti sub-layer, leading to the propagation of cracks and fracture in coating under erosion impact. As a result, the G1 sample displayed the high erosion rates at 0.095 ± 0.0048 mg/g and 0.099 ± 0.0383 mg/g both for 90° and 30° erosive angles. However, inserting the soft Ti sub-layer within G1 coating structure not only enhanced the adhesion strength but decreased the residual stress, which could further suppress the fracture and delamination of multilayer coating for G2 sample. As a result, the G2 sample illustrated the improved erosion resistance under various incident angles. The G3 sample, which had well-balanced residual stress and load-bearing capacity, owned the lowest erosion rate (0.060 ± 0.0002 mg/g at 90° and 0.024 ± 0.0068 mg/g at 30°) for the proper thickness of the Ti layer. As the Ti layer became thicker, the thickness of TiN layer decreased and the

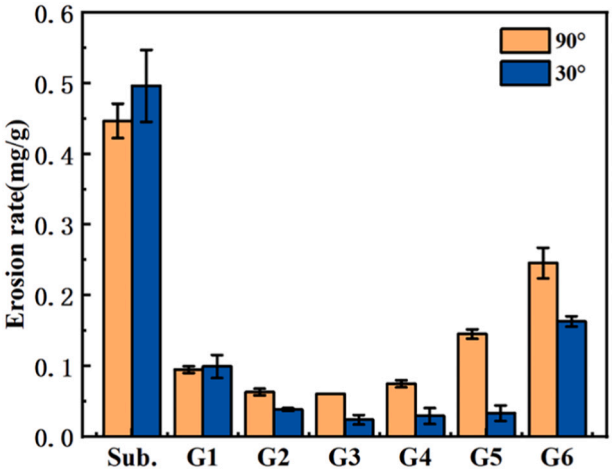

Fig. 12. Erosion rates of the substrates and the Ti/TiN/TiAlN multilayer coatings eroded by silica sand at 90° and 30°.

erosion rate of the G4 sample and the G5 sample increased in both 90° and 30°. Besides, the erosion rate of the G5 sample (0.145 ± 0.0067 mg/g) surpassed that of the G1 sample at the erosion angle of 90°, which ascribed the poor load-bearing capacity of the coating. The G6 sample exhibited the worst erosion resistance for all erosion angles, where the erosion rate was 0.246 ± 0.0217 mg/g at 90° and 0.163 ± 0.0074 mg/g at 30°. This could be ascribed to the poorest load-bearing capacity with severe deformation of coating, which accelerated the emerge and propagation of cracks under erosion impacts. In other words, the existence of TiN sublayer within coating might be of great importance to enhance the erosion resistance. Combined with the above discussion, it could be concluded that the adhesion strength, residual stress, hardness and load-bearing capacity of the coating played an important role in erosion damage under high erosion angle. The TiN transition layer was indispensable in improving the erosion resistance of the coatings by guaranteeing the load-bearing capacity of the coatings.

As a consequence, the G3 sample had the best comprehensive performance, which could achieve excellent erosion performance with a good combination of high hardness, proper residual stress, high adhesion strength, good crack resistance, and well load-bearing capacity in multilayer coatings consisting of hard and ductile layers.

Fig. 13 presents the morphologies of the G3 sample after erosion test at the erosion angle of 90° and 30°. Compared to the sample eroded at 30°, the surface morphologies of the sample eroded at 90° suffered from more severe damage. As shown in Fig. 13(a), apart from erosion pits were observed, large eroded area indicated hard coatings performed poor under high erosion angle. Fracture and brittle chipping events were attributed to high brittleness of the upper TiAlN layer (Fig. 13(b)), which remained to be ameliorating. When the erosion angle was 30°, only small erosion pits could be detected and the surface of the coating kept intact (Fig. 13(c)). Besides, the surface of the coating was covered with reticular cracks (Fig. 13(d)), which also indicated the high brittleness of the upper TiAlN layer. It indicated that the toughness of the TiAlN layer urgently needed to be improved in the succeeding study.

To investigate the failure evolution of coatings eroded under 90° and 30°, the cross-sectional morphologies of the G3 sample after eroded is shown in Fig. 14. Under the erosion angle of 90°, plastic deformation was clearly observed in Fig. 14(a)-(b). Radical cracks initiated at the Ti/TiN interface in most cases (Fig. 14(a)-(b)) and lateral cracks were

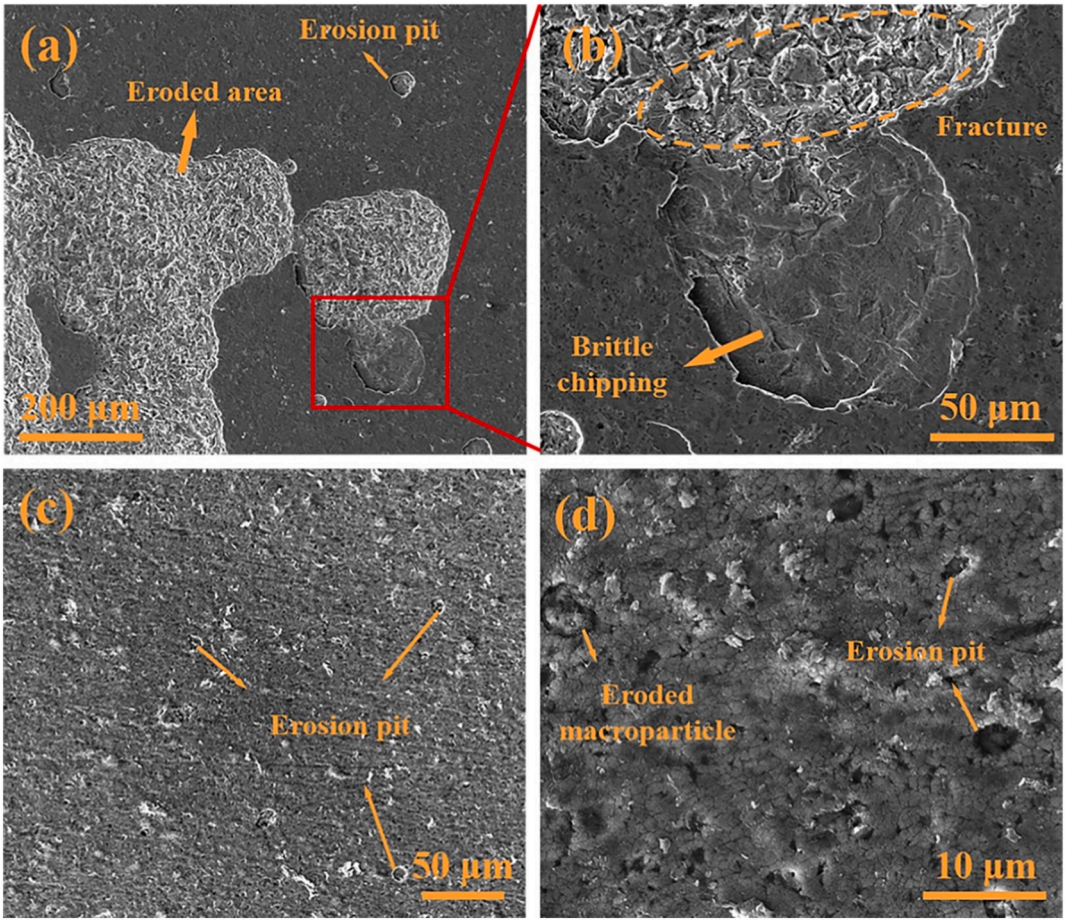

Fig. 13. Morphologies of the G3 sample after erosion: (a) (b) 90°, (c) (d) 30°.

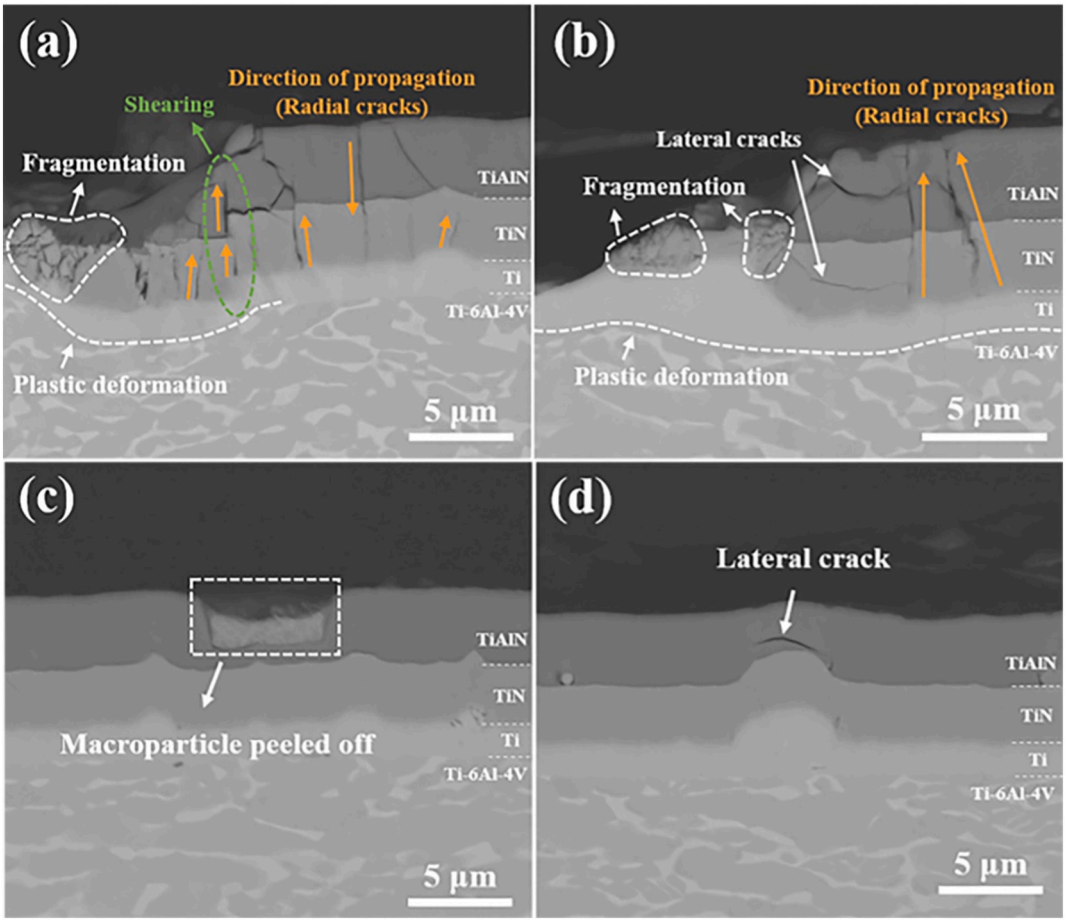

Fig. 14. Cross-sectional morphologies of the G3 sample after erosion: (a) (b) 90°, (c) (d) 30°.

occurred in the TiN and TiAlN layers (Fig. 14(b)). Besides, lateral cracks caused by shearing events were detected at the TiN/TiAlN interface in Fig. 14(a), where significant plastic deformation occurred. When the TiAlN top layer was consumed, the exposed TiN layer rapidly fragmented, indicating the importance of the TiAlN layer. Consequently, the coating failure could be clarified from the combined effect of delamination and fracture within the multilayer structure. Under the strong erosion impact of 90°, the delamination occurred firstly between TiAlN layer and TiN layer, which was followed by the subsequently fracture appearance in TiN layer with loss of Ti layer. Once the TiAlN top layer was exhausted under severe erosion impact, the fracture became the dominated factor for coating failure. More importantly, the gradual expansion of eroded area in multilayer coating was further stimulated with the alternative erosion impacts. Under the erosion angle of 30°, only pits, which formed after the peeling off of macroparticles, were observed (Fig. 14(c)) and lateral cracks occurred in the TiAlN layer (Fig. 14(d)), where was affected by the macroparticles.

4. Conclusions

The Ti/TiN/TiAlN multilayer coatings were deposited on Ti-6Al-4V substrates by a self-designed multisource cathodic arc ion deposition system. The crack resistance and erosion resistance of the coatings were investigated using scratch tests and home-made erosion rig, respectively. The hardness, elastic modulus, load-bearing capacity and residual stress of the coatings gradually decreased and the adhesion strength increased firstly and then decreased with the thickness of the Ti layer increasing. The G3 sample (T_{Ti}:T_{TiN} = 1:2) exhibited the best comprehensive properties by the proper combination of hardness, residual stress, adhesion strength, crack resistance, load-bearing capacity and erosion resistance. The ductile Ti layer in the multilayer coatings not only provided strong adhesion strength between the coatings and substrates, but also coordinated the deformation between the soft substrates and hard TiN/TiAlN layers and absorbed strain energy during the deformation process. What's more, the ductile Ti layer could reduce the residual stress and the TiN layer was indispensable in maintain the load-bearing capacity of the coatings and vital as a transition layer in coordinating the hardness gap of Ti and TiAlN layer. The amelioration of the toughness of the TiAlN layer and the improvement of the transition of Ti/TiN interface need to be optimized in the future.

Credit authorship contribution statement

Z.Y. Wang and A.Y. Wang conceived and supervised the project; H.T. Ruan designed and carried out the experiments under the supervision of Z.Y. Wang and A.Y. Wang; L. Wang and L.L. Sun helped to carry out XRD and SEM measurements; H. Peng and P.L. Ke help to perform the erosion experiment and analyze the erosion mechanism; H.T. Ruan wrote the manuscript; All authors discussed the results and commented on the manuscript.

Declaration of competing interest

The authors declare that they have no known competing financial interests or personal relationships that could have appeared to influence the work reported in this paper.

Acknowledgement

This research was supported by the National Science and Technology

Major Project (2017-VII-0012-0108), National Natural Science Foundation of China (52025014, 51901238), and Ningbo Municipal Natural Science Foundation (202003N4025).

References

[1] I. Finnie, Erosion of surfaces by solid particles, Wear 3 (1960) 87–103, https://doi.org/10.1016/0043-1648(60)90055-7.

[2] R. Kurz, K. Brun, Degradation of gas turbine performance in natural gas service, J. Nat. Gas Sci. Eng. 1 (2009) 95–102, https://doi.org/10.1016/j.jngse.2009.03.007.

[3] A. Hamed, W. Tabakof, R. Wenglarz, Erosion and deposition in turbomachinery, J. Propuls. Power 22 (2006) 350–360, https://doi.org/10.2514/1.18462.

[4] R. Rajendran, Gas turbine coatings – an overview, Eng. Fail. Anal. 26 (2012) 355–369, https://doi.org/10.1016/j.engfailanal.2012.07.007.

[5] J.T. Demasi-Marcin, D.K. Gupta, Protective coatings in the gas turbine engine, Surf. Coat. Technol. 68–69 (1994) 1–9, https://doi.org/10.1016/0257-8972(94)90129-5.

[6] G.W. Goward, Progress in coatings for gas turbine airfoils, Surf. Coat. Technol. 108–109 (1998) 73–79, https://doi.org/10.1016/S0257-8972(98)00667-7.

[7] E. Bousser, L. Martinu, J.E. Klemberg-Sapieha, Solid particle erosion mechanisms of protective coatings for aerospace applications, Surf. Coat. Technol. 257 (2014) 165–181, https://doi.org/10.1016/j.surfcoat.2014.08.037.

[8] V.P. Swaminathan, R. Wei, D.W. Gandy, Nanotechnology coatings for erosion protection of turbine components, J. Eng. Gas Turb. Power 132 (2010), 082014, https://doi.org/10.1115/1.3028567.

[9] K.J. Ma, A. Bloyce, T. Bell, Examination of mechanical properties and failure mechanisms of TiN and Ti−TiN multilayer coatings, Surf. Coat. Technol. 76–77 (1995) 297–302, https://doi.org/10.1016/0257-8972(95)02585-5.

[10] B. Borawski, J.A. Todd, J. Singh, D.E. Wolfe, The influence of ductile interlayer material on the particle erosion resistance of multilayered TiN based coatings, Wear 271 (2011) 2890–2898, https://doi.org/10.1016/j.wear.2011.06.004.

[11] M. Naveed, A. Obrosov, S. WEIß, Investigation of the Wear resistance properties of Cr/CrN multilayer coatings against sand erosion, conference papers, Science 2015 (2015), 873543, https://doi.org/10.1155/2015/873543.

[12] P. Wieciński, J. Smolik, H. Garbacz, K.J. Kurzydłowski, Erosion resistance of the nanostructured Cr/CrN multilayer coatings on Ti6Al4V alloy, Vacuum 107 (2014) 277–283, https://doi.org/10.1016/j.vacuum.2014.02.024.

[13] V. Bonu, M. Jeevitha, V.P. Kumar, G. Srinivas, H.C. Barshilia, Solid particle erosion and corrosion resistance performance of nanolayered multilayered Ti/TiN and TiAl/TiAlN coatings deposited on Ti6Al4V substrates, Surf. Coat. Technol. 387 (2020), 125531, https://doi.org/10.1016/j.surfcoat.2020.125531.

[14] J. Gu, L. Li, M. Ai, Y. Xu, G. Li, D. Deng, H. Peng, S. Luo, P. Zhang, Improvement of solid particle erosion and corrosion resistance using TiAlSiN/Cr multilayer coatings, Surf. Coat. Technol. 402 (2020), 126270, https://doi.org/10.1016/j.surfcoat.2020.126270.

[15] J. Shuai, X. Zuo, Z. Wang, P. Guo, B. Xu, J. Zhou, A. Wang, P. Ke, Comparative study on crack resistance of TiAlN monolithic and Ti/TiAlN multilayer coatings, Ceram. Int. 46 (2020) 6672–6681, https://doi.org/10.1016/j.ceramint.2019.11.155.

[16] R. Wei, E. Langa, J. Arps, Q. Yang, L. Zhao, Erosion resistance of thick nitride and carbonitride coatings deposited using plasma enhanced magnetron sputtering, Plasma Process. Polym. 4 (2007) s693–s699, https://doi.org/10.1002/ppap.200731707.

[17] V.S. Sergevnin, I.V. Blinkov, D.S. Belov, N.I. Smirnov, A.O. Volkhonskii, K. A. Kuptsov, Wear and erosion of arc-PVD multilayer Ti-Al-Mo-N coatings under various conditions of friction and loading, Int. J. Adv. Manuf. Technol. 98 (2018) 593–601, https://doi.org/10.1007/s00170-018-2235-z.

[18] V. Shibe, V. Chawla, Erosion studies of cermet-coated ASTM A36 steel, Ind. Lubr. Tribol. 71 (2019) 242–252, https://doi.org/10.1108/ILT-01-2018-0001.

[19] A.C. Vlasveld, S.G. Harris, E.D. Doyle, D.B. Lewis, W.D. Munz, Characterisation and performance of partially filtered arc TiAlN coatings, Surf. Coat. Technol. 149 (2002) 217–224, https://doi.org/10.1016/S0257-8972(01)01448-7.

[20] Q. Yang, R. Mckellar, Nanolayered CrAlTiN and multilayered CrAlTiN–AlTiN coatings for solid particle erosion protection, Tribol. Int. 83 (2015) 12–20, https://doi.org/10.1016/j.triboint.2014.11.002.

[21] H. Zhang, Z. Li, W. He, B. Liao, G. He, X. Cao, Y. Li, Damage evolution and mechanism of TiN/Ti multilayer coatings in sand erosion condition, Surf. Coat. Technol. 353 (2018) 210–220, https://doi.org/10.1016/j.surfcoat.2018.08.062.

[22] J. Shuai, X. Zuo, Z. Wang, L. Sun, R. Chen, L. Wang, A. Wang, P. Ke, Erosion behavior and failure mechanism of Ti/TiAlN multilayer coatings eroded by silica sand and glass beads, J. Mater. Sci. Technol. 80 (2021) 179–190, https://doi.org/10.1016/j.jmst.2021.01.001.

[23] L.A. Dobrzański, K. Lukaszkowicz, Erosion resistance and tribological properties of coatings deposited by reactive magnetron sputtering method onto the brass substrate, J. Mater. Process. Technol. 157–158 (2004) 317–323, https://doi.org/10.1016/j.jmatprotec.2004.09.050.

[24] X. Cao, W. He, B. Liao, H. Zhou, H. Zhang, C. Tan, Z. Yang, Sand particle erosion resistance of the multilayer gradient TiN/Ti coatings on Ti6Al4V alloy, Surf. Coat. Technol. 365 (2019) 214–221, https://doi.org/10.1016/j.surfcoat.2018.08.066.

[25] H. Zhang, Z. Li, C. Ma, W. He, X. Cao, Y. Li, The anti-sand erosion performance of TiN films fabricated by filtered cathodic vacuum arc technique at different nitrogen flow rates, Ceram. Int. 45 (2019) 10819–10825, https://doi.org/10.1016/j.ceramint.2019.02.157.

[26] X. Cao, W. He, G. He, B. Liao, H. Zhang, J. Chen, C. Lv, Sand erosion resistance improvement and damage mechanism of TiAlN coating via the bias-graded voltage in FCVA deposition, Surf. Coat. Technol. 378 (2019), 125009, https://doi.org/10.1016/j.surfcoat.2019.125009.

[27] J.R. Laguna-Camacho, L.A. Cruz-Mendoza, J.C. Anzelmetti-Zaragoza, A. Marquina-Chávze, M. Vite- Torres, J. MartÍnez-Trinidad, Solid particle erosion on coatings employed to protect die casting molds, Prog. Org. Coat. 74 (2012) 750–757, https://doi.org/10.1016/j.porgcoat.2011.09.022.

[28] J.S. Grewal, B.S. Sidhu, S. Prakash, High temperature erosion performance of nanostructured and conventional TiAlN coatings on AISI-304 boiler steel substrate, T. Indian I. Metals 67 (2014) 889–902, https://doi.org/10.1007/s12666-014-0413-8.

[29] Q. Yang, D.Y. Seo, L.R. Zhao, X.T. Zeng, Erosion resistance performance of magnetron sputtering deposited TiAlN coatings, Surf. Coat. Technol. 188–189 (2004) 168–173, https://doi.org/10.1016/j.surfcoat.2004.08.012.

[30] J. Deng, F. Wu, Y. Lian, Y. Xing, S. Li, Erosion wear of CrN, TiN, CrAlN, and TiAlN PVD nitride coatings, Int. J. Refract. Met. Hard Mater. 35 (2012) 10–16, https://doi.org/10.1016/j.ijrmhm.2012.03.002.

[31] H. Cao, F. Qi, X. Ouyang, N. Zhao, Y. Zhou, B. Li, W. Luo, B. Liao, J. Luo, Effect of ti transition layer thickness on the structure, mechanical and adhesion properties of ti-DLC coatings on aluminum alloys, Materials 11 (2018), https://doi.org/10.3390/ma11091742.

[32] W.C. Oliver, G.M. Pharr, An improved technique for determining hardness and elastic modulus using load and displacement sensing indentation experiments, J. Mater. Res. 7 (1992) 1564–1583, https://doi.org/10.1557/JMR.1992.1564.

[33] Y. Kawakami, M. Watanabe, K. Arai, S. Sugimoto, Effects of substrate materials on piezoelectric properties of BaTiO3 thick films deposited by aerosol deposition, Jpn. J. Appl. Phys. 55 (2016), https://doi.org/10.7567/JJAP.55.10TA10.

[34] A.D. Pogrebnjak, V.M. Beresnev, O.V. Bondar, B.O. Postolnyi, K. Zaleski, E. Coy, S. Jurga, M.O. Lisovenko, P. Konarski, L. Rebouta, J.P. Araujo, Superhard CrN/MoN coatings with multilayer architecture, Mater. Des. 153 (2018) 47–59, https://doi.org/10.1016/j.matdes.2018.05.001.

[35] R. Ali, M. Sebastiani, E. Bemporad, Influence of Ti–TiN multilayer PVD-coatings design on residual stresses and adhesion, Mater. Des. 75 (2015) 47–56, https://doi.org/10.1016/j.matdes.2015.03.007.

[36] K.H. Kim, S.H. Lee, Comparative studies of TiN and Ti1−xAlxN by plasma-assisted chemical vapor deposition using a TiCl4/AlCl3/N2/H2/Ar gas mixture, Thin Solid Films 283 (1996) 165–170, https://doi.org/10.1016/0040-6090(96)08766-4.

[37] O. Çomaklı, Improved structural, mechanical, corrosion and tribocorrosion properties of Ti45Nb alloys by TiN, TiAlN monolayers, and TiAlN/TiN multilayer ceramic films, Ceram. Int. 47 (2021) 4149–4156, https://doi.org/10.1016/j.ceramint.2020.09.292.

[38] R. Saha, W.D. Nix, Effects of the substrate on the determination of thin film mechanical properties by nanoindentation, Acta Mater. 50 (2002) 23–38, https://doi.org/10.1016/S1359-6454(01)00328-7.

[39] J.Y. Zhang, X. Zhang, R.H. Wang, S.Y. Lei, P. Zhang, J.J. Niu, G. Liu, G.J. Zhang, J. Sun, Length-scale-dependent deformation and fracture behavior of Cu/X (X=Nb, Zr) multilayers: the constraining effects of the ductile phase on the brittle phase, Acta Mater. 59 (2011) 7368–7379, https://doi.org/10.1016/j.actamat.2011.08.016.

[40] D. Gross, T. Seelig, Fracture Mechanics, Second Ed., Springer, Berlin, 2011.

[41] A. Azizpour, R. Hahn, F.F. Klimashin, T. Wojcik, E. Poursaeidi, P.H. Mayrhofer, Deformation and cracking mechanism in CrN/TiN multilayer coatings, Coatings 9 (2019) 363, https://doi.org/10.3390/coatings9060363.

[42] C.K.H. Dharan, B.S. Kang, I. Finnie, Finnie's Notes on Fracture Mechanics, Springer, New York, 2016.